Computer Methods and Programs in Biomedicine 151 (2017) 21–32

Contents lists available at ScienceDirect

Computer Methods and Programs in Biomedicine

journal homepage: www.elsevier.com/locate/cmpb

ARC–OCT: Automatic detection of lumen border in intravascular OCT images

Grigorios-Aris Cheimariotis[a,b,1], Yiannis S. Chatzizisis[c,1], Vassilis G. Koutkias[b,a,1], Konstantinos Toutouzas[d], Andreas Giannopoulos[e], Maria Riga[d], Ioanna Chouvarda[a,b], Antonios P. Antoniadis[f], Charalambos Doulaverakis[g], Ioannis Tsamboulatidis[g], Ioannis Kompatsiaris[g], George D. Giannoglou[h], Nicos Maglaveras[a,b,*]

[a] *Lab of Computing Medical Informatics and Biomedical Imaging Technologies, Medical School, Aristotle University of Thessaloniki, Thessaloniki, Greece*
[b] *Institute of Applied Biosciences, Center for Research and Technology - Hellas, Thermi, Thessaloniki, Greece*
[c] *Cardiovascular Division, University of Nebraska Medical Center, Omaha, Nebraska, USA*
[d] *1st Department of Cardiology, Athens Medical School, Hippokration Hospital, Athens, Greece*
[e] *Applied Imaging Science Lab, Radiology Department, Brigham and Women's Hospital, Harvard Medical School, Massachusetts, USA*
[f] *Cardiovascular Division, Brigham and Women's Hospital, Harvard Medical School, Boston, Massachusetts, USA*
[g] *Information Technologies Institute, Center for Research and Technology - Hellas, Thermi, Thessaloniki, Greece*
[h] *1st Department of Cardiology, AHEPA University Hospital, Medical School, Aristotle University of Thessaloniki, Thessaloniki, Greece*

ARTICLE INFO

Article history:
Received 4 November 2016
Revised 29 July 2017
Accepted 8 August 2017

Keywords:
Intravascular optical coherence tomography (OCT)
Lumen–Endothelium border
Automatic segmentation
Contour extraction

ABSTRACT

Background and Objective: Intravascular optical coherence tomography (OCT) is an invaluable tool for the detection of pathological features on the arterial wall and the investigation of post-stenting complications. Computational lumen border detection in OCT images is highly advantageous, since it may support rapid morphometric analysis. However, automatic detection is very challenging, since OCT images typically include various artifacts that impact image clarity, including features such as side branches and intraluminal blood presence. This paper presents ARC–OCT, a segmentation method for fully-automatic detection of lumen border in OCT images.
Methods: ARC–OCT relies on multiple, consecutive processing steps, accounting for image preparation, contour extraction and refinement. In particular, for contour extraction ARC–OCT employs the transformation of OCT images based on physical characteristics such as reflectivity and absorption of the tissue and, for contour refinement, local regression using weighted linear least squares and a 2nd degree polynomial model is employed to achieve artifact and small-branch correction as well as smoothness of the artery mesh. Our major focus was to achieve accurate contour delineation in the various types of OCT images, i.e., even in challenging cases with branches and artifacts.
Results: ARC–OCT has been assessed in a dataset of 1812 images (308 from stented and 1504 from native segments) obtained from 20 patients. ARC–OCT was compared against ground-truth manual segmentation performed by experts on the basis of various geometric features (e.g. area, perimeter, radius, diameter, centroid, etc.) and closed contour matching indicators (the Dice index, the Hausdorff distance and the undirected average distance), using standard statistical analysis methods. The proposed method was proven very efficient and close to the ground-truth, exhibiting non statistically-significant differences for most of the examined metrics.
Conclusions: ARC–OCT allows accurate and fully-automated lumen border detection in OCT images.

1. Introduction

Intravascular optical coherence tomography (OCT) is an established diagnostic tool that enables the visualization of the internal aspect of the coronary arteries with very high resolution [1]. It is highly accurate for the detection of features of coronary disease and the investigation of post-stenting complications [2].

* Corresponding author at: Lab. of Computing and Medical Informatics, Medical School, Aristotle University of Thessaloniki, P.O. Box 323, 54124, Thessaloniki, Greece.
E-mail address: nicmag@med.auth.gr (N. Maglaveras).
[1] The first three authors contributed equally to the manuscript.

http://dx.doi.org/10.1016/j.cmpb.2017.08.007

OCT segmentation for lumen border detection is a key step in the quantitative assessment of arterial morphology [3,4]. Manual tracing of the lumen contours is laborious and time consuming given the large number of images acquired in a typical OCT examination (i.e., usually more than 200 in a single pullback). Automatic OCT segmentation is anticipated to enable significantly faster (near real-time) morphometric analyses of OCT frames compared to manual segmentation; however, this task is quite challenging, since OCT images typically contain various elements that impact image clarity and induce artifacts, including side branches and intraluminal blood [5,6]. While segmentation of ophthalmic OCT images has been extensively elaborated [7–12], recently some efforts focused on the analysis of OCT images [13–21]. Even though those algorithms are promising, their performance varies significantly due to the above OCT-specific image characteristics.

In this paper, we present ARC–OCT, a method for fully automatic detection of the lumen border in OCT images. ARC–OCT relies on a multi-step segmentation procedure that applies on real-world OCT images, including those with anatomic variations or artifacts, which are often excluded from relevant studies [13], and have been recognized as a major challenge [14–16]. In summary, ARC–OCT employs a series of image transformations, e.g., taking into account reflectivity and absorption of tissue, which leads to a binary image and helps to identify regions with different intensity features in the original image as parts of the arterial wall (white areas). The luminal contour in a radial scan (the so-called A-line) is located at the point where the scan (starting from the catheter) meets a bright shape (i.e., a transition from black to white). Once the initial assessment of the internal contour is performed, artifacts are corrected by applying a smoothing function on the curve, which represents the internal contour. Next, side branches of the vessel are identified with statistical control of the curve slope and, finally, the contour is re-estimated on the respective regions. Using a large set of OCT images from native and stented arterial segments, we compared ARC–OCT with manual segmentation (conducted by expert cardiologists) corresponding to the ground-truth. Comparisons were made on the basis of various geometric and closed-contour similarity features.

The paper is structured as follows. In Section 2 we discuss related works, while in Section 3 we refer to the material of the study. Section 4 presents thoroughly ARC–OCT, while Section 5 presents the evaluation metrics and the obtained results. In Section 6 we discuss the outcomes and the limitations of the current study, future work directions, and the conclusions of this study.

2. Related work

Various works that attempted the same automatic segmentation task rely on the morphology of binary image, resulting from the application of a threshold to a preprocessed image. Preprocessing concerns mainly smoothing filters. For example, Gurmeric et al. [17] selected 50% of the histogram as threshold, while Bourezak et al. [18] used a threshold that varies smoothly in each A-scan. Athanasiou et al. [19] and Celi et al. [20] applied a global Otsu threshold, while Moraes et al. [15] applied also a global Otsu threshold to the matrix of coefficient of approximation that comes from performing one-level decomposition to the preprocessed image. The main difference of ARC–OCT is that instead of applying a threshold to the original image or to the matrix of coefficient of approximation, it applies Otsu threshold to a transformed image provided by the image gradient window and the OCT-specific processing steps.

Sihan et al. [21] proposed an algorithm that uses multiple Canny filters to detect edges as well as a heuristic method to exclude some and link other into lumen contour. Quite differently and focused on contour extraction from stented images, Ughi et al. [14] detected the point of the endothelium border before the point of maximum intensity of the A-scan, moving from the catheter towards the endothelium. Each A-line was classified as: (a) empty (corresponding to open branch), (b) “clear” (where only normal tissue is found), or (c) stent-line, based on measurements depending on the intensity profile of the A-scan. After classification, the stent was segmented in stent-strut lines and the tissue was segmented in clear lines. If the A-line was clear, the point of the endothelium border was detected before the point of maximum intensity of the A-scan, moving from the catheter towards the endothelium. Contrary to the method of Ughi et al., which employed manual removal of guide wire artifacts before segmentation, ARC–OCT is fully automated and it does not focus on stent segments only.

Overall, the main difference of ARC–OCT compared to methods which render the image binary, lies in the transformations provided by the image gradient window and the formula that is used to highlight the more reflective parts of tissue. These are performed before applying a global threshold, offering the advantage to deal with a significant number of images with shaded parts of lumen. ARC–OCT also incorporates post-processing steps for correcting contours in images with artifacts and/or branches.

Besides being fully-automated or not and the differences in particular analysis steps, another point of ARC–OCT discrimination compared to other methods concerns their validation. This typically considered only one metric, i.e. the area of the lumen in each cross-section, which was compared with the area of the manual segmentation by experts. In order to assure the reliability of our findings, the ARC–OCT validation performed in the current study relied on a variety of metrics and indices, both geometric and closed contour matching indicators, using standard statistical analysis methods.

Equally important, quantitative results presented in relevant methods illustrated that in various types of cases segmentation is far from optimal, thus, the need for further research as proposed by ARC–OCT.

3. Material

Our study was based on 1812 images, obtained from 20 coronary arteries [LAD (left anterior descending artery), $n = 14$; LCX (left circumflex artery), $n = 1$; RCA (right coronary artery), $n = 5$; mean length $= 39.7 \pm 10.0$ mm], of patients who underwent a clinically indicated cardiac catheterization and OCT. From these images, 308 corresponded to stented arterial segments. A representative OCT image of the elaborated set is presented in Fig. 1. Images were acquired with a Frequency Domain OCT imaging system (FD-OCT C7-XRT OCT Intravascular Imaging System, Westford, MA, USA). The pullback speed was 20 mm/s, the axial resolution was 15 μm, and the frame rate was 100 frames/s. Temporary blood clearance was achieved with contrast injection. Manual segmentation of these images has been performed and assessed with a high degree of agreement among experts [22]. The study was approved by the Institutional Ethics Committee and the subjects provided written informed consent for their participation.

4. ARC–OCT: automatic detection of lumen border

ARC–OCT consists of the following analysis workflow: (1) image preparation including artifact/noise reduction and image transformations, (2) core contour extraction, taking into account generic image features and OCT-specific characteristics, and (3) contour refinement involving smoothing and contour corrections. Each of these phases includes further analysis steps, as illustrated in Fig. 2 and described below.

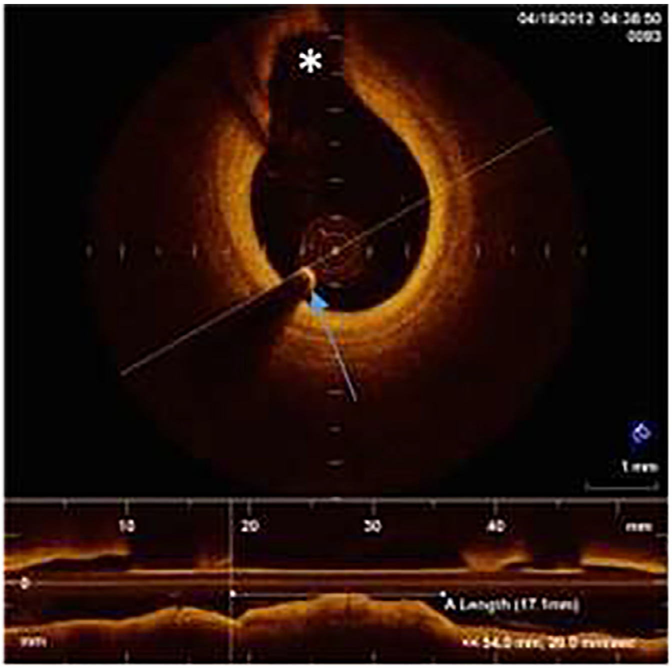

Fig. 1. Sample OCT image of the elaborated image set. The asterisk indicates a branch, and the arrow a guide wire artifact. A thorough documentation of the artifacts that may be found in OCT is presented in [5] (and in its respective online supplementary material).

4.1. Image preparation

4.1.1. Removal of calibration markers

The catheter reflection and the calibration marks in the original images (Fig. 3(a)) can be considered as noise, thereby affecting the segmentation accuracy. Since these features have specific location, dimensions, and characteristics, they were removed by applying local, image-specific median filters (Fig. 3(B)).

4.1.2. Removal of speckle noise

This step was applied to achieve uniformity of image regions. Images were normalized and a 2D median filter (5×5 window) was applied to completely attenuate the effect of alignment marks that could be still present. Then, a Gaussian filter was applied (5×5 window, $\sigma = 2.5$), followed by an image opening operation applied in a disk containing 13 neighbors as structuring element, in order to further smoothen the image without blurring/affecting borders and to render image parts in a uniform way (Fig. 3(c)) [23].

4.1.3. Image conversion into grayscale and polar coordinates

Representation of the images in polar coordinates facilitates the visualization of local image regions in terms of their radial and tangential characteristics (Fig. 3(d)). In our case, this transformation is favorable for the analysis of the intensity profile of individual A-lines. Given a pixel (x,y) in the Cartesian domain, its correspondent (ρ,θ) in polar coordinates is given by:

$$x = C_x + \rho * \cos(\theta) \text{ and } y = C_y + \rho * \sin(\theta), \quad (1)$$

where (C_x,C_y) is the image center coordinates in the Cartesian domain.

4.2. Core contour extraction

4.2.1. Image gradient window

A smoother version of image gradient is given by the regional gradient that was calculated by subtracting the mean intensity in a rectangular window (of size 10×5) above a pixel (ρ,θ) from the mean intensity in a rectangular window (again 10×5) below the pixel. If I is the input image of this step, then $Ireg$ is the image with intensity in each of its points equal to the image gradient of I:

$$Ireg(\rho,\theta) = \frac{1}{(2d\theta+1)d\rho} * \left(\sum_{i=-d\theta}^{d\theta} \sum_{j=1}^{d\rho} I(\rho+j,\theta+i) - \sum_{i=-d\theta}^{d\theta} \sum_{j=-d\rho}^{1} I(\rho+\theta,\theta+i) \right). \quad (2)$$

Although typically used to detect edges, in our case this transformation helped classifying pixels in homogeneous regions as background parts rather than possible parts of the wall, while pixels on borders between homogeneous regions of different intensity were enhanced or less attenuated. This enhancement was important to compensate for the effect of the next analysis step to discriminate two image structures, i.e., shaded areas and candidate boundaries. The size of the window was experimentally determined by the need to give a significant extent to the points enhanced "row-wise" and to emphasize on the difference "column-wise".

4.2.2. OCT-specific processing (transforming from intensity to reflectivity)

This is a key step in ARC–OCT, which helps detecting the contour in special conditions. Different tissue types have different

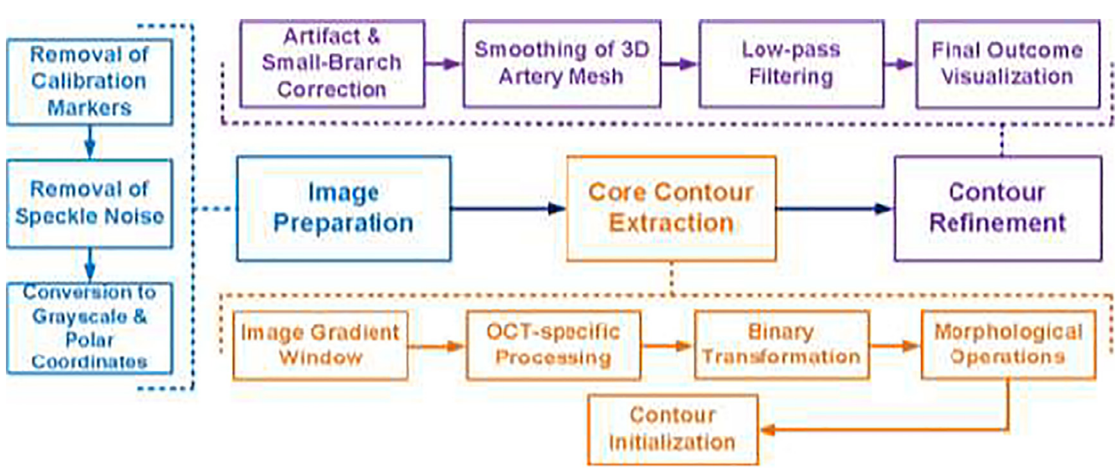

Fig. 2. The employed image processing workflow for OCT lumen border extraction (main phases along with their intermediate steps).

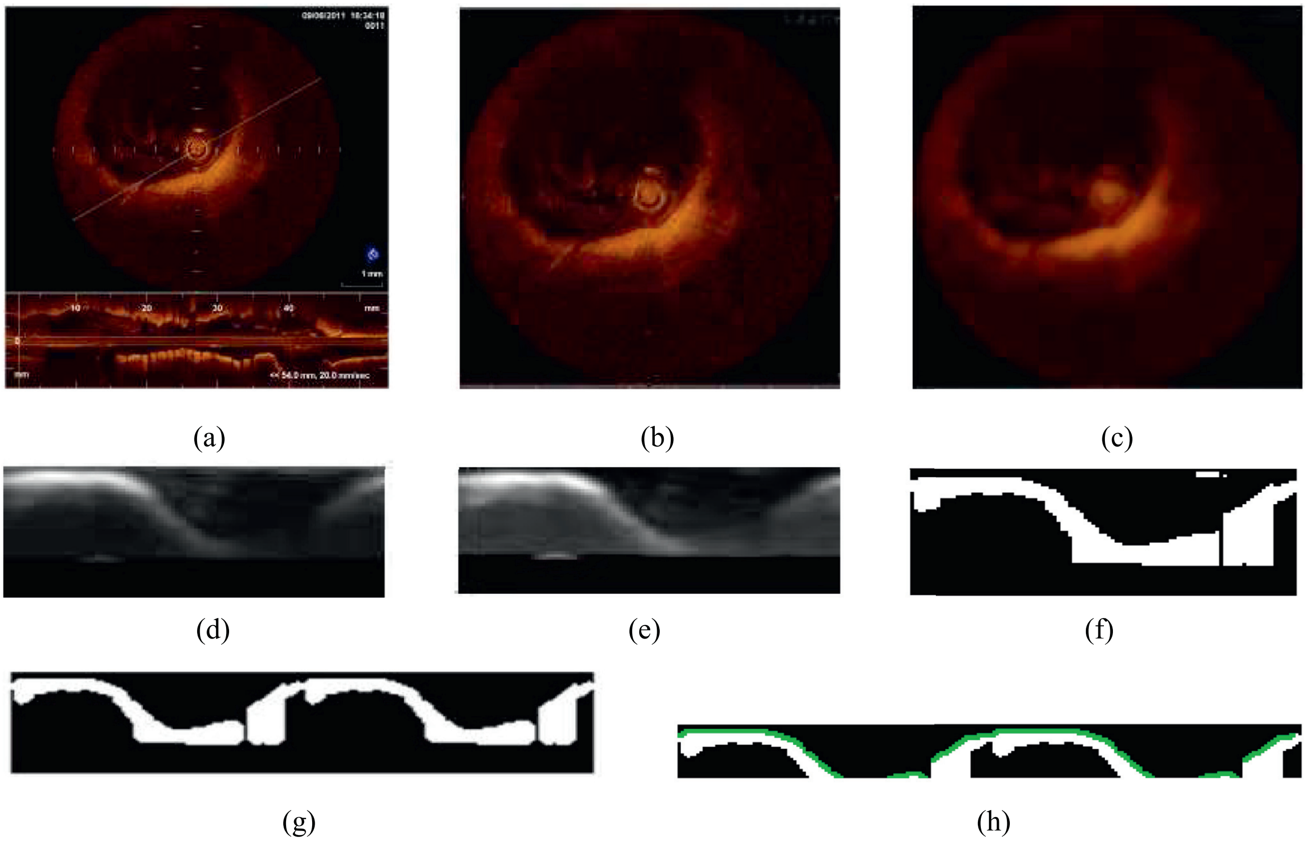

Fig. 3. Image preparation and core contour extraction: (a) input image, (b) removal of calibration markers, (c) removal of speckle noise and image opening, (d) transformation of grayscale image into polar coordinates, (e) OCT-specific processing (transformation from intensity to reflectivity), (f) binary image transformation, (g) morphological operations, and (h) contour initialization.

properties in terms of absorption and backscattering of light [5]. In particular, light absorption results in shaded areas, thus, “hiding” lumen edge, while backscattering is greater when the tissue reflectance is high [3]. The intensity value of a pixel is the product of illumination and reflectance. As endothelium has the highest value of reflectance, a transformation was applied to the image, in order to detect areas possibly containing tissue, even if these were shaded (Fig. 3(e)). The key idea of the transformation is to enhance any pixel that is preceded by pixels (moving from the catheter towards the artery wall in the same angle) of high intensity which indicates that it may be shaded by a highly reflective artifact. The *Ibgn* coefficient provides a value of luminosity that is greater than background pixel values [24]. In particular, if *Ireg* is the outcome image of the previous steps and $Ireg(\rho,\theta) > Ibgn$, then the resulting image *Iref* is given by:

$$Iref(\rho,\theta) = Ireg(\rho,\theta) * \max(Ireg/Ibgn) * \left(\sum_{i=1}^{i=\rho} Ireg(i,\theta) \Big/ \sum_{i=1}^{\iota=N} Ireg(i,\theta)\right), \quad (3)$$

while if $Ireg(\rho,\theta) \leq Ibgn$, then $Iref(\rho,\theta)=0$, where N is the number of rows in the image matrix.

The first term max(Ireg/Ibgn) is constant for each image and helps to balance intensities in the whole image, to be in suitable range for the thresholding step that follows. The second term $\sum_{i=1}^{i=\rho} Ireg(I,\theta) / \sum_{i=1}^{\iota=N} Ireg(I,\theta)$ is the sum of intensities of the pixels that are in the same angle θ and are closer to the catheter than the pixel whose value is adjusted, divided by the sum of intensities of all the pixels in the same angle. For example, along an A-scan, and in pixels above background threshold, this term would be higher in an artery wall pixel when preceded by an artifact than when not, and also along an artifact free A-scan, it would increase with distance from catheter, compensating for absorption.

Parameters (like IT) employed in ARC–OCT, along with their values, are summarized in Table 1. The parameter values were initially determined by visual inspection. In a next phase, the values have been fine-tuned based on the overall performance of the algorithm which was evaluated by the similarity (measured by the mean dice index) of the automatic segmentation results and the manual contours (gold standard).

Table 1
Optimal parameter values for ARC–OCT.

Parameter	Description	Value	Analysis Step Employed
Ibgn	Approximation of maximum intensity of image background	6	4.2.2 OCT-specific Processing
IT	Intensity threshold for binarization	0.10	4.2.3 Binary Transformation
Nr	Threshold number of connected pixels	50	4.2.4 Morphological Operations
OT1	Outlier threshold applied on the difference of radius between consecutive points of the contour	20	4.3.1 Artifact and Small Branch Correction
OT2	Outlier threshold for outlier presence	10	4.3.2 Smoothing of 3D artery mesh
Q	Haar filters parameter	3	4.3.3 Low-pass Filtering

4.2.3. Binary transformation

In order to discriminate the background from areas of interest, we adopted a local Otsu binarization process, applied on each column representing an A-scan [24]. The result was an image which is white in the respective regions of interest of the original image and black where the background of the original image is (Fig. 3(f)). Otsu is a dynamic threshold selection method, in which a histogram is divided into two classes by seeking for minimal intraclass and maximal interclass variance. Hence, a good separation for data with bimodal histogram is provided. In our case, some columns corresponded to empty lines, i.e., dark lines (usually because of an open branch) that had no information about where the tissue could be.

Due to the transformations described previously, non-significant parts of the image obtained a certain low-intensity value that discriminated them from the background in an empty line. If the Otsu threshold was applied, it would be calculated at a very low value, rendering some parts of the A-scan white. Instead of that, we chose to render that column black, if the value of the Otsu threshold was below an intensity threshold (*IT*), which was set 10% of the maximum intensity of the image.

4.2.4. Morphological operations

This step removed small objects and disjoint white areas, so that artifacts could be distinguished from the tissue (Fig. 3(g)). Image opening was applied with a disk containing 13 neighbors as structuring element. Then, subtraction of small areas that consist of less than *Nr* white pixels (*Nr* is proportional to the image size) was applied, because these areas are considered artifacts.

4.2.5. Contour initialization

For a first estimation of the targeted contour, in each column we chose as the initial contour point the first transition from black to white of the second shape that an A-line meets moving from the catheter to the artery wall (Fig. 3(h)).

In case there was only one shape, we chose the first transition overall (Fig. 3(h)). Initialization points between empty areas, where no initialization took place, were connected with a straight line. The initial contour comprised of a set of pixels:

$$C = \{p = [\rho,\ \theta]\}, \tag{4}$$

where θ is the value of the column of the image matrix that corresponds to an A-scan and ρ is the value of the row of the image matrix. Considering that the pixels of the contour were ordered for consecutive angles, if θ was the angle of pixel p_i, then $\theta + 1$ was the angle of pixel p_{i+1}.

4.3. Contour refinement

4.3.1. Artifact and small-branch correction

This step removed outliers or areas of extreme values due to small branches or artifacts. Let *C*' be the outcome of applying a smoothing function to *C*, which consisted of a moving average filter. In particular, local regression using weighted linear least squares and a 2nd degree polynomial model was employed [25]. The function assigned 0 weight to data outside:

$$mean(\rho) + 6 * SD(\rho), \tag{5}$$

with *SD* the standard deviation. As it was possible to lose accuracy by extensive smoothing, we considered the presence of outliers only when:

$$\left|\rho_i - -\rho_i{'}\right| > OT1, \tag{6}$$

where ρ_i' is the radius of *C*', ρ_i is the radius of *C* for the same angle θ_i, and *OT1* is an outlier threshold. In this case, we considered pixel ρ_i as wrongly determined. After removing all outlier pixels by following this procedure, we estimated the new ones based on the adjacent parts (Fig. 4(d)–(e)). This step succeeds in correcting artifacts and branches when they appear as outliers in the contour *C*.

4.3.2. Smoothing of 3D artery mesh

Since there are cases with branches and artifacts where the contour *C* is smooth and so is contour *C*', the correction was not possible with the previous step. Therefore, an analogous correction is used that takes advantage of the information from other slices. The contours of consecutive slices that are part of the same artery, create a mesh *M*. The lines *L* that consist of mesh points that correspond to a specific angle θ are smoothed by applying the same moving average filter as in the previous step, resulting in *L*' new lines. We considered the presence of outliers when:

$$\left|\rho_i - \rho_i{'}\right| > OT2, \tag{7}$$

where ρ_i' is the radius of *L*', ρ_i is the radius of *L* for the same angle θ_i, and *OT2* is an outlier threshold.

4.3.3. Low-pass filtering

There are cases where the resulting contours *C* do not have the smoothness that the vessel was expected to have. To assure that every extracted contour is smooth, a low-pass filtering procedure took place based on consecutive Haar filters, as applied in [26], i.e., $H(z^{2i})$, with $i\epsilon[0, Q\text{-}1]$ and:

$$H(z) = \frac{1}{2}\left(1 + z^{-1}\right) \tag{8}$$

These filters were successively applied to the contour function.

4.3.4. Final outcome visualization

This final step transformed the image from polar to Cartesian coordinates, incorporating the extracted contour and superimposing it in the original image.

5. Results

The contours extracted by ARC–OCT were compared with the contours that were manually defined by clinical experts, constituting the gold standard in our study. We made a separate analysis for stented and non-stented arterial regions, given that OCT is extensively used for the early identification of post-stenting complications and the fact that stented images introduce different types of image features and artifacts. Comparisons were performed by calculating shape metrics applied on a frame-by-frame basis. These metrics involved geometric features of the detected contour, i.e., the area (in mm^2), the perimeter (in mm), the min and max radius (in mm), the min and max diameter (in mm), and the centroid point (coordinates in mm). Besides geometric features, we employed additional indicators for comparing closed contours, namely, the Dice index (value range [0,1], with 1 denoting the perfect match among contours) [27], the Hausdorff distance [28], and the undirected average distance (UAD). The Hausdorff distance and UAD are measured in mm, and a zero value denotes the perfect fit among the compared contours. All the above metrics and indicators were employed to assess the match between the contours extracted by ARC–OCT and the manually-defined contours.

Fig. 5 depicts boxplots of the Dice index, the Hausdorff distance, and UAD, respectively, for both non-stented and stented segments compared to manual segmentation. ARC–OCT presented low values for Hausdorff distance and UAD. Contour distance measures presented similar median value and distribution in stented and non-stented images. Similarly, the results for the Dice index were close to 1. For a more in-depth analysis regarding the agreement between ARC–OCT and manual segmentation, Figs. 6

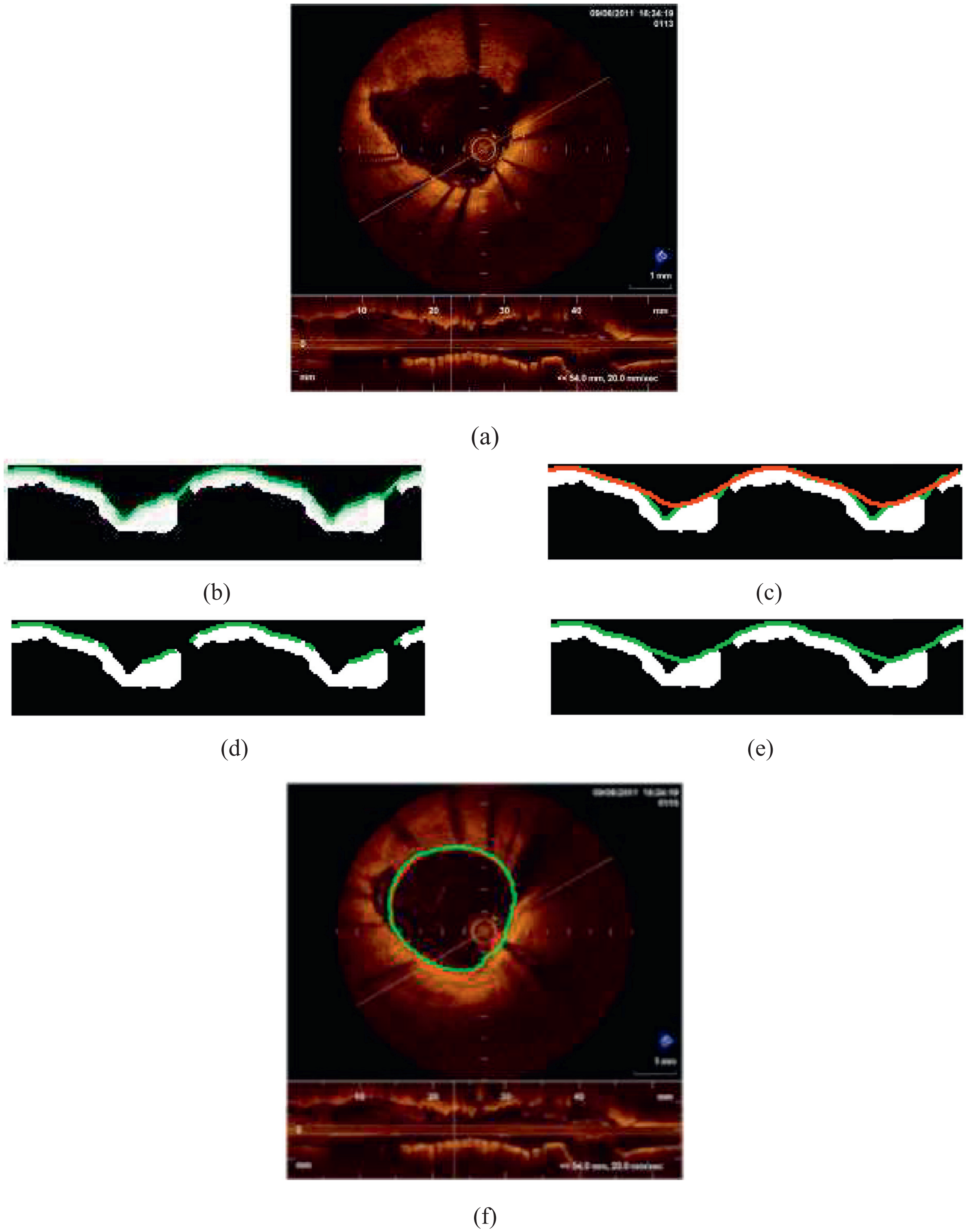

Fig. 4. Contour refinement: (a) example input image, (b) contour estimation in empty A-scans, (c) newer estimation by a smooth function (red line), (d) correction (contour depicted in (b) without the part that differs significantly from the smooth contour depicted in (c)), (e) re-estimation of contour in empty A-scans, and (f) output image. (For interpretation of the references to color in this figure legend, the reader is referred to the web version of this article.)

and 7 depict the respective Bland–Altman analysis plots for all the geometrical features [29], for non-stented and stented images, respectively. In addition, Table 2 illustrates the results obtained through linear regression analysis. In all cases Bland–Altman plots showed a small bias and narrow limits of agreement. Linear regression analysis showed a significantly high correlation $R^2 > 0.88$, $p < 0.001$ for both stented and non-stented images, and average error less than ± 0.1 mm (or mm^2 for the area) in all cases, except area ($\sim -0.18\ mm^2$) and perimeter (~ -0.4 mm). Perimeter underestimation without respective area significant underestimation might have been related to different smoothing of contours.

As a comparison of ARC-OCT with manual segmentation for both stented and non-stented segments, Table 3 presents the values for the median and the 25%, 75% quartiles for the

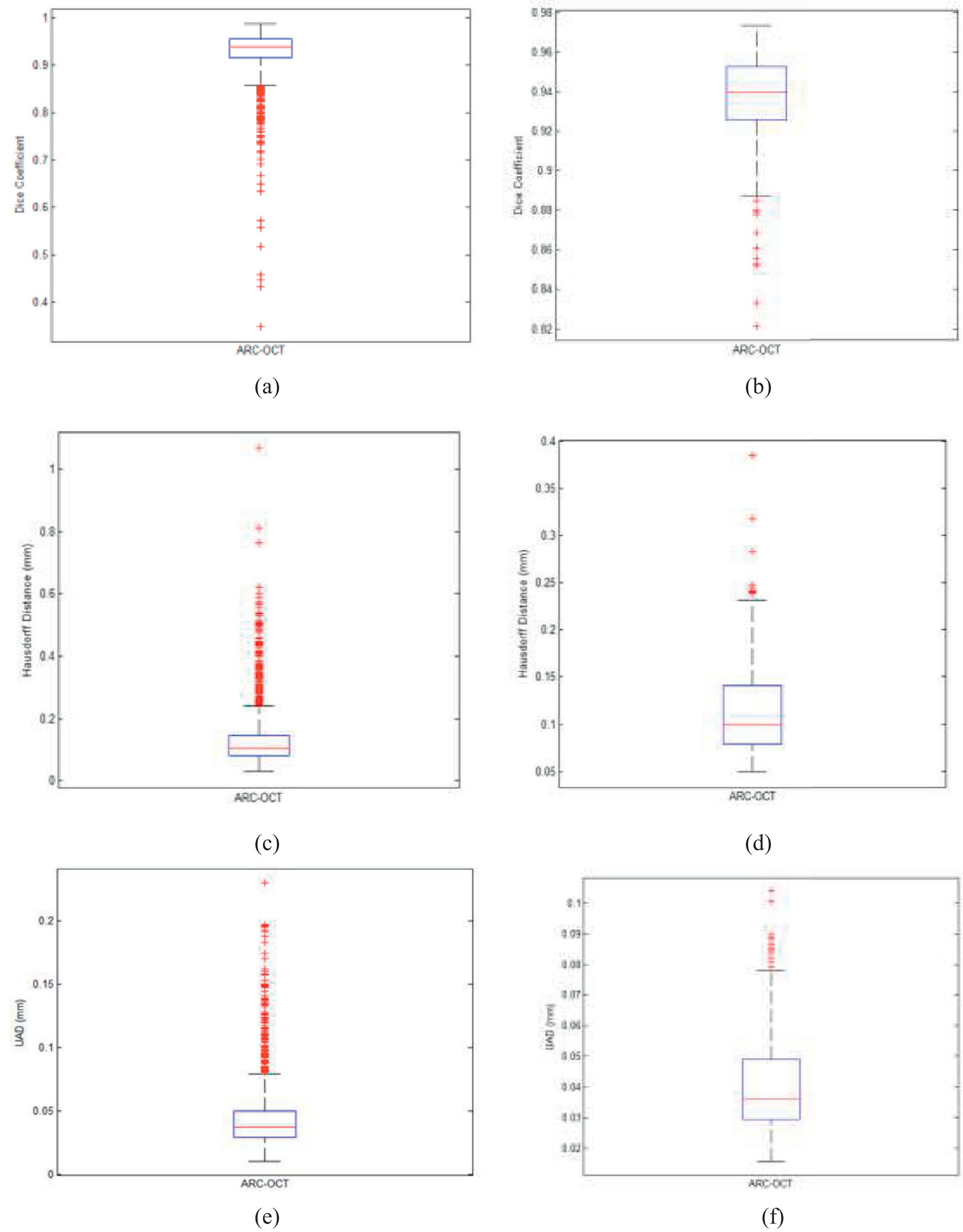

Fig. 5. Boxplots of: (a)–(b) the Dice index, (c)–(d) the Hausdorff distance, and (e)–(f) the UAD for the contours extracted by ARC–OCT (left column: non-stented images; right column: stented images).

calculated geometrical metrics. It compares ARC–OCT with manual segmentation in terms of statistical significance in the differences of these metrics, using as significance threshold *p*-value < 0.001. Non-parametric rank sum testing was employed to test for medians equality. As shown in Table 3, ARC–OCT was very close to manual segmentation. In particular, regarding the median, in non-stented segments ARC–OCT was close to the ground-truth for all eight measures. In stented segments, ARC–OCT was close to the ground-truth in three measures, while for stented segments ARC–OCT did not exhibit statistically significant differences with the ground-truth in three of the employed measures, suggesting its high segmentation performance.

Concerning time performance, the algorithm can segment a single slice in less than a second, without applying 3D smoothing, which is suitable for real time inspection. If the input to the algorithm is a series of slices (>=2), 3D smoothing is performed. The entire process takes less than a minute when including smoothing of 3D artery mesh in a series of 100 slices.

Fig. 8 depicts representative lumen detection examples performed by ARC–OCT in both stented and non-stented segments. As

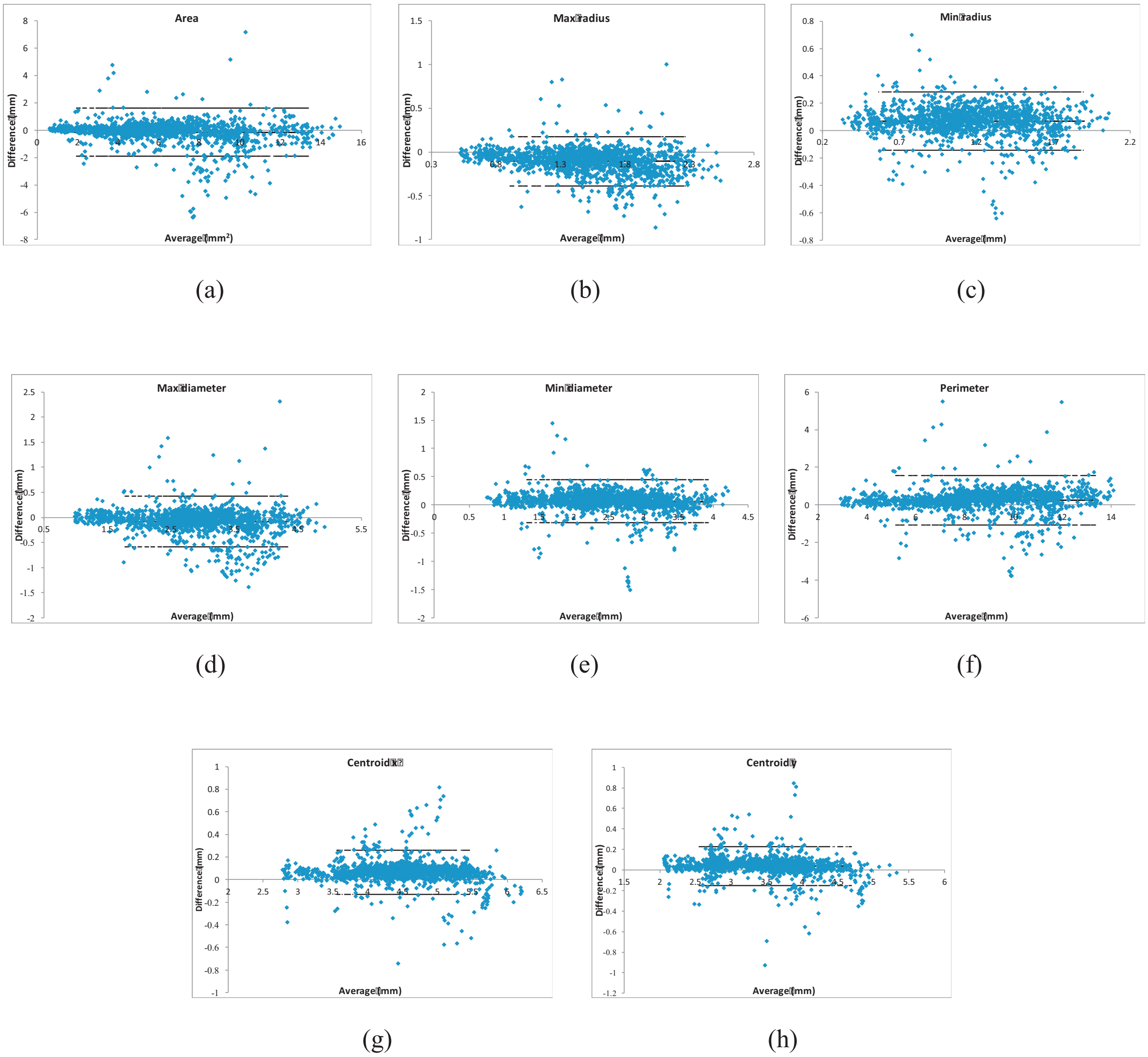

Fig. 6. Non-stented images: Bland–Altman plots of differences between manual and ARC–OCT segmentation (y-axis) against their mean (x-axis) for all geometric metrics. The middle horizontal line represents the mean difference, while marginal horizontal lines represent the limits of agreement (mean ± 1.96SD).

Table 2
Agreement between ARC–OCT and manual segmentation.

Evaluation Measure	Linear Regression Equation	R^2	Bias (average error estimation)	p-value
Area (mm^2)	$y = 1.0x + 0.09/y = 0.88x + 0.48$	0.92/0.97	0.14/−0.18	<0.001
Maximum radius (mm)	$y = 1.02x + 0.08/y = 0.88x + 0.24$	0.88/0.93	0.10/0.07	<0.001
Minimum radius (mm)	$y = 0.97x - 0.03/y = 0.87x + 0.04$	0.91/0.93	−0.07/−0.07	<0.001
Maximum diameter (mm)	$y = x + 0.08/y = 0.88x + 0.33$	0.89/0.95	0.08/0.02	<0.001
Minimum diameter (mm)	$y = 0.99x - 0.05/y = 0.90x + 0.15$	0.93/0.96	−0.07/−0.1	<0.001
Perimeter (mm)	$y = 0.95x + 0.21/y = 0.84x + 0.94$	0.92/0.96	−0.24/−0.41	<0.001
Centroid x (mm)	$y = x - 0.06/y = 1.08x - 0.45$	0.98/0.98	−0.06/−0.03	<0.001
Centroid y (mm)	$y = 1.01x - 0.07/y = x - 0.01$	0.98/0.99	−0.03/0	<0.001

Remarks: (a) A/B notation: A corresponds to the results between non-stented images and B to the stented images, respectively; (b) $p < 0.001$ refers to both non-stented and stented images.

it is shown, ARC–OCT is accurate even in cases of poor image quality.

6. Discussion and conclusion

In this study we presented ARC–OCT, a method for fully-automatic detection of lumen borders in OCT images. Our major goal was to develop a method capable of segmenting real-world OCT images containing stented segments, branches, and artifacts [2,5,6]. Especially for evaluating stent expansion, thrombosis, and malapposition, OCT is the method of choice both in clinical and research settings [30]. Hence, accurate automated segmentation on such artery areas is crucial for further evaluation of OCT images.

ARC–OCT allows accurate and fully-automated lumen border detection in OCT images. Its underlying algorithm includes a series of processing steps spanning from image transformations to contour extraction based on morphological operations and OCT-specific characteristics, and contour refinements. The accuracy of ARC–OCT was successfully assessed using multiple geometric and close-contour matching criteria in a large dataset of 1812 images,

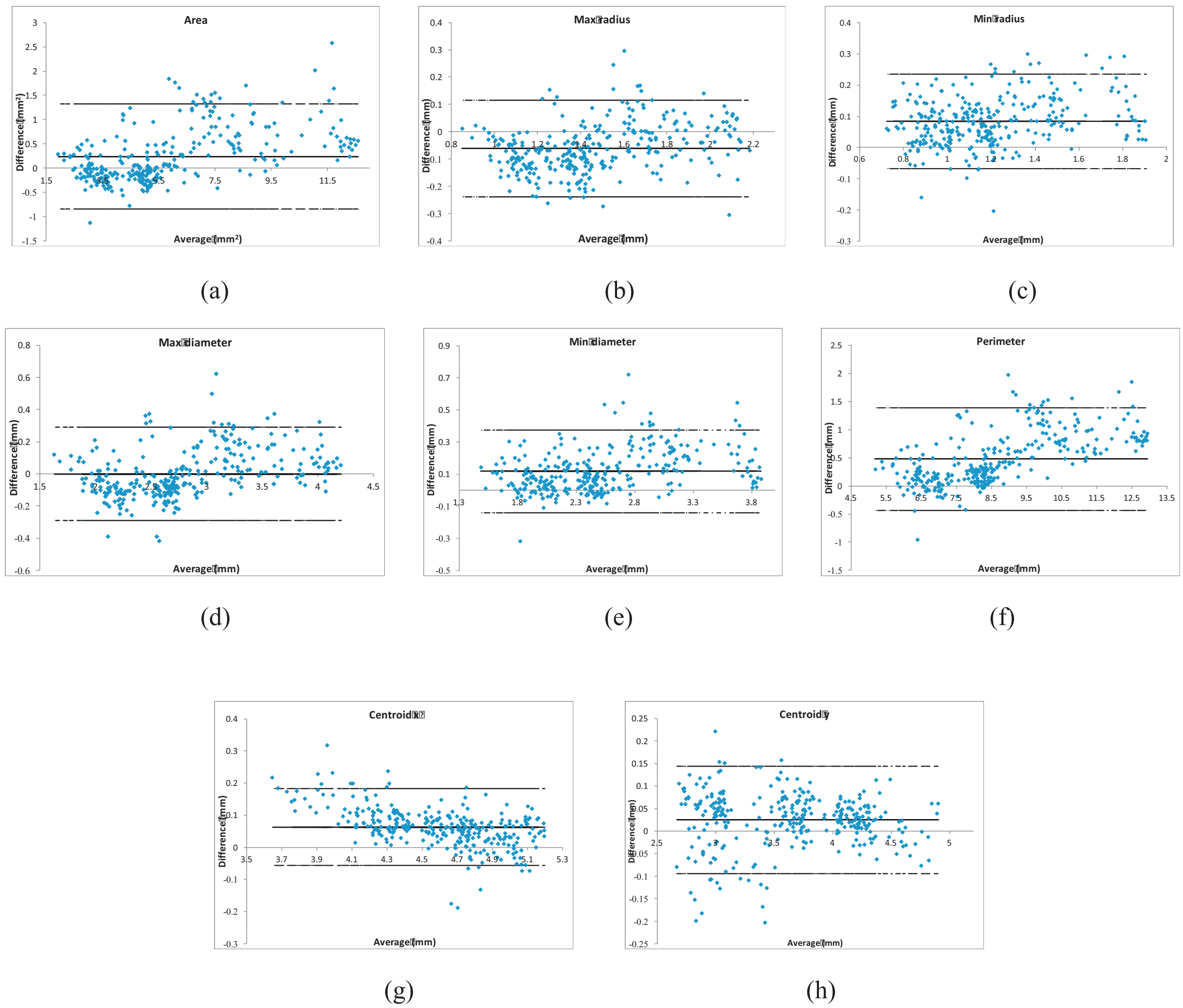

Fig. 7. Stented images: Bland–Altman plots of differences between manual and ARC–OCT segmentation (y-axis) against their mean (x-axis) for all geometric metrics. The middle horizontal line represents the mean difference, while marginal horizontal lines represent the limits of agreement (mean ± 1.96SD).

Table 3
Comparison of evaluation measures between manual segmentation and ARC–OCT.

Evaluation Measure	25%	Median	75%	p-value
Area (mm^2)	4.01/3.77	5.52/5.18	8.31/6.81	0.32/ 0.75
	3.94/3.61	5.52/5.09	7.96/7.81	
Maximum radius (mm)	1.33/1.26	1.56/1.45	1.89/1.67	<0.001/0.03
	1.23/1.17	1.48/1.36	1.75/1.68	
Minimum radius (mm)	0.89/0.95	1.11/1.12	1.38/1.31	<0.001/<0.01
	0.97/1.00	1.18/1.19	1.45/1.42	
Maximum diameter (mm)	2.48/2.34	2.92/2.74	3.53/3.15	0.05/0.43
	2.40/2.26	2.88/2.66	3.44/3.28	
Minimum diameter (mm)	1.96/2.04	2.39/2.41	2.95/2.76	0.09/0.02
	2.05/2.09	2.48/2.46	3.00/3.04	
Perimeter (mm)	7.27/7.04	8.52/8.19	10.34/9.37	0.004/<0.001
	7.46/7.08	8.84/8.42	10.58/10.46	
Centroid x (mm)	4.04/4.29	4.50/4.62	4.93/4.85	<0.001/0.048
	4.18/4.36	4.61/4.68	5.00/4.86	
Centroid y (mm)	2.90/3.03	3.53/3.66	3.87/4.14	0.04/0.40
	3.02/3.09	3.57/3.69	3.91/4.17	

Remark: A/B notation: A corresponds to the results between non-stented images and B to the stented images, respectively.

both stented and non-stented, obtained from 20 patients. Comparisons were made with the ground-truth manual segmentation, illustrating that ARC–OCT is highly efficient and close to the ground-truth in the majority of the examined cases. To this end, ARC–OCT has the potential to facilitate OCT segmentation enabling rapid morphometric analyses in native and stented arterial segments.

Various methods have been proposed for automatic OCT segmentation (as presented in the Related Work section). We made a series of comparisons of ARC–OCT with relevant methods, in particular with those presented in Ughi et al. [14] and Moraes et al. [15], and ARC–OCT presents advantages over them. The implementation of these methods is not publicly available and, thus,

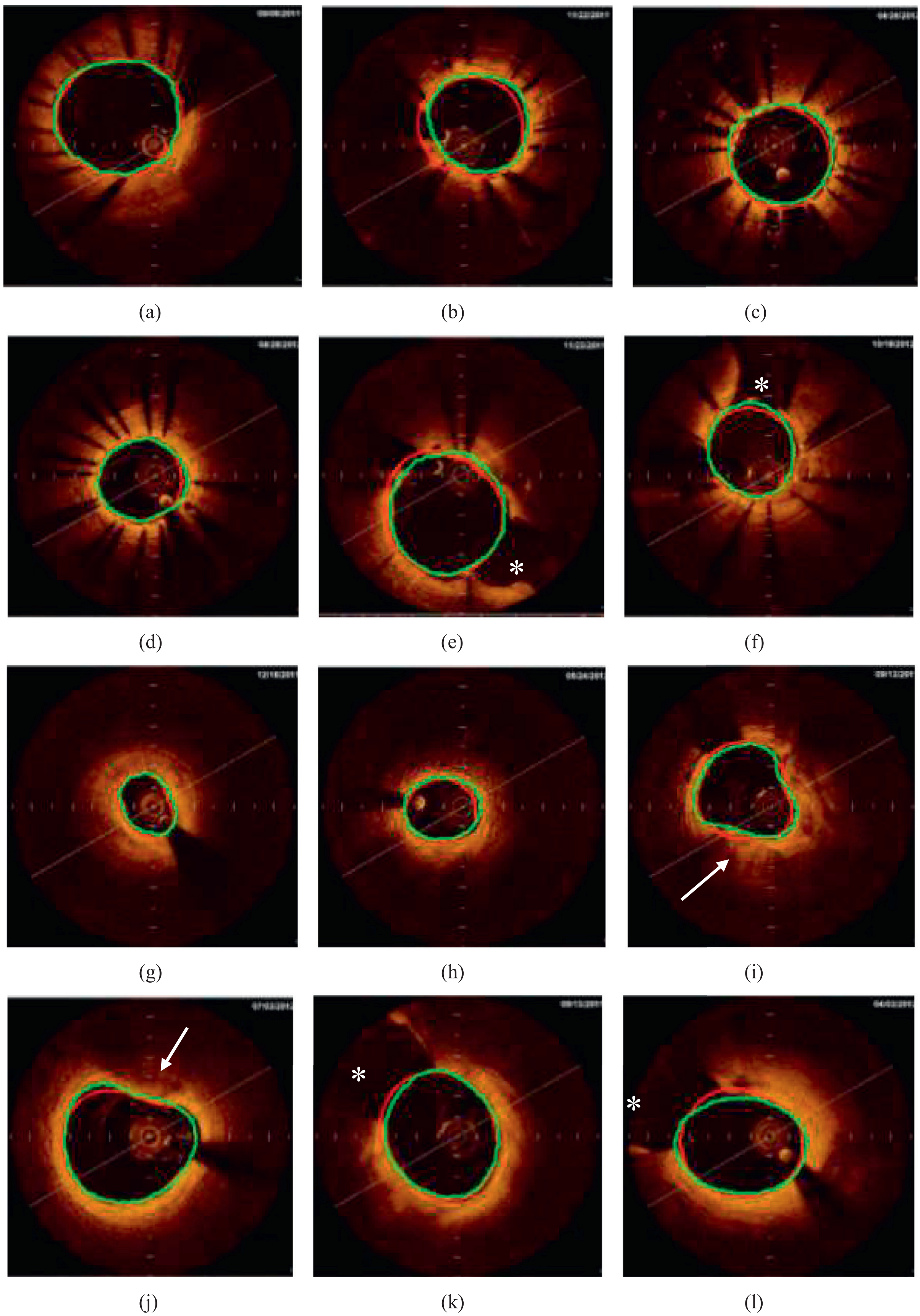

Fig. 8. Indicative segmentation outcomes obtained from ARC-OCT. Red contour corresponds to the ARC-OCT outcome and green to manual segmentation. (a)–(g) correspond to stented images, while (h)–(l) to non-stented images. (a), (b), (g) and (h) represent OCT frames without artifacts. (c), (d) represent OCT frames with guide wire artifact. In (i) and (j) presence of atherosclerotic plaques (fibrocalcific and fibrous with lipid pool, respectively) is indicated with an arrow. In (e), (f), (k) and (l) presence of side branches is indicated with *. All the outcomes of ARC-OCT present high agreement with the manual segmentation. (For interpretation of the references to color in this figure legend, the reader is referred to the web version of this article.)

Table 4
Overview of results presented by various automatic methods.

Method	Test set size	Specific info	Kind of test set	Metrics	Value of metric
Gurmeric et al	39 cross-sections	Stented	Intracoronary OCT	Bland–Altman (Area)	0.11 ± 0.70 mm^2
Moraes et al (5.9 ± 3 s)	90 images	Included images with a variety of artifacts	Intravascular OCT from 2 patients, 2 pigs, and 1 rabbit	Dice	0.971
				Dice of the method implemented by our team in ARC–OCT dataset	0.844 non-stented, 0.881 stented
Athanasiou et al.	556 images randomly selected from 22 patients	Excluded frames with any kind of artifact	Intracoronary OCT	Bland-Altman(Area) limits of agreement	$-0.080 \pm 1.96 \times 0.082$ mm^2
				Pearson correlation coefficient	0.99
				Positive predictive value (PPV)	0.98
Celi et al.	Validation set 210 images (randomly selected)	Included images with common artifacts and common difficult imaging conditions	Intracoronary OCT	Limits of agreement (Area)	1.2 mm^2
				Correlation coefficient	0.97 and 0.96 (two different manual delineations as gold standard)
Tsantis et al.	2710 images	Stented and non-Stented	Human Femoral Artery	Overlap(Dice)	0.937 ± 0.045
Sihan et al. (3–5 s)	4137 images.	In 3% of the detected contours an observer correction was necessary.	Intracoronary OCT	Mean lumen areas human vs. automated	5.2 ± 2.16 mm^2 (manual) 5.1 ± 2.21 mm^2 (automatic) $P = 0.26$
				Regression analysis r	0.99
ARC-OCT (1 s)	1812 images from 20 pull-backs	No exclusions	Intracoronary OCT	Dice	0.935 (stented), 0.925 (non-stented)
				R^2 (Area)	0.97(stented), 0.92 (non-stented)

having accurate information regarding the implementation details of these methods was not possible, while necessary for a reliable comparison. To this end, since our implementations of other published methods (which were based on the content of the respective papers per se) might be questionable, this could make our comparative evaluation results questionable as well. For this reason, we provide Table 4 with information about the results that other methods present in different datasets. In the same table, we choose to present for our method, the same metrics that are commonly used by other methods. It is obvious that the comparison is still a difficult task since all other methods present fewer metrics than our method and also the metrics used differ for each method. Most importantly, it is difficult to compare because many of these methods are validated in much smaller data set and in some occasions there are exclusions of challenging images. However, it can be observed that only our method is validated against a large dataset of human intracoronary images with no exclusions and no observer corrections and that it presents equally accurate results with other methods. Since, exclusion of challenging images, observer corrections and small datasets improve significantly metrics value, it can be argued that ARC–OCT is more accurate. For example, our implementation of Moraes et al method validated against the data set used to validate ARC–OCT, has a mean dice 0.844 for non-stented images and 0.881 for stented images, while the results in their paper imply a mean dice index of 0.97.

ARC–OCT builds upon our previous work [22], which focused on: (a) the construction of an annotated OCT imageset by engaging experts in the manual definition of lumen borders, and (b) the clinical validation of a first approach for automatic OCT segmentation, which finally suggested a semi-automatic method for lumen border detection. Extending this prior work, ARC–OCT is fully automated by employing OCT-specific features enabling accurate contour extraction and handling of discontinuities. All comparisons were performed against the ground-truth in terms of various geometric metrics and closed contour comparison indicators and by conducting standard statistical analysis methods. In almost all features, ARC–OCT was found very close to the ground-truth, for both stented and native segments.

As future work, we consider employing contour information extracted from consecutive frames as an extra constraint in the segmentation. Given the high accuracy of ARC–OCT, we aim to introduce it both into the clinical environment and as a research tool. Our goal is to follow an approach similar to [31] and integrate ARC–OCT in a graphical tool aiming to facilitate 3D reconstruction of coronary arteries. An accurate 3D arterial model will enable the performance of advanced computational fluid dynamics studies [32], in order to assess the implication of local hemodynamics in atherosclerosis and in-stent restenosis.

Conflict of interest

The authors have no conflicts of interest to declare.

References

[1] M.E. Brezinski, Current capabilities and challenges for optical coherence tomography as a high-impact cardiovascular imaging modality, Circulation 123 (25) (2011) 2913–2915.

[2] H.G. Bezerra, M.A. Costa, G. Guagliumi, A.M. Rollins, D.I. Simon, Intracoronary optical coherence tomography: a comprehensive review: clinical and research applications, JACC Cardiovasc. Interv. 2 (11) (2009) 1035–1046.

[3] A. Giannopoulos, Y.S. Chatzizisis, G.D. Giannoglou, Optical coherence tomography: an arrow in our quiver, Expert Rev. Cardiovasc. Ther. 10 (5) (2012) 539–541.

[4] I.K. Jang, B.E. Bouma, D.H. Kang, S.J. Park, S.W. Park, K.B. Seung, et al., Visualization of coronary atherosclerotic plaques in patients using optical coherence tomography: comparison with intravascular ultrasound, J. Am. Coll. Cardiol. 39 (4) (2002) 604–609.

[5] G.J. Tearney, E. Regar, T. Akasaka, T. Adriaenssens, P. Barlis, H.G. Bezerra, et al., Consensus standards for acquisition, measurement, and reporting of intravascular optical coherence tomography studies: a report from the international

working group for intravascular optical coherence tomography standardization and validation, J. Am. Coll. Cardiol. 59 (12) (2012) 1058–1072.
[6] F. Prati, E. Regar, G.S. Mintz, E. Arbustini, C. Di Mario, I.K. Jang, et al., Expert review document on methodology, terminology, and clinical applications of optical coherence tomography: physical principles, methodology of image acquisition, and clinical application for assessment of coronary arteries and atherosclerosis, Eur. Heart J. 31 (4) (2010) 401–415.
[7] P.A. Dufour, L. Ceklic, H. Abdillahi, S. Schroder, S. De Dzanet, U. Wolf, Schnurrbusch, et al., Graph-based multi-surface segmentation of OCT data using trained hard and soft constraints, IEEE Trans. Med. Imaging 32 (3) (2013) 531–543.
[8] R. Kafieh, H. Rabbani, F. Hajizadeh, M. Ommani, An accurate multimodal 3-D vessel segmentation method based on brightness variations on OCT layers and curvelet domain fundus image analysis, IEEE Trans. Biomed. Eng. 60 (10) (2013) 2815–2823.
[9] K.A. Vermeer, J. van der Schoot, H.G. Lemij, J.F. de Boer, Automated segmentation by pixel classification of retinal layers in ophthalmic OCT images, Biomed. Opt. Express 2 (6) (2011) 1743–1756.
[10] Y. Huang, Development of a semi-automatic segmentation method for retinal OCT images tested in patients with diabetic macular edema, PLoS One 8 (12) (2013) e82922 Dec 26.
[11] H. Ishikawa, D.M. Stein, G. Wollstein, S. Beaton, G.J. Fujimoto, J.S. Schuman, Macular segmentation with optical coherence tomography, Invest Ophthalmol. Vis. Sci. 46 (6) (2005) 2012–2017.
[12] F. Rathke, S. Schmidt, C. Schnörr, Probabilistic intra-retinal layer segmentation in 3-D OCT images using global shape regularization, Med. Image Anal. 18 (5) (2014) 781–794.
[13] S. Tanimoto, G. Rodriguez-Granillo, P. Barlis, S. de Winter, N. Bruining, R. Hamers, et al., A novel approach for quantitative analysis of intracoronary optical coherence tomography: high inter-observer agreement with computer-assisted contour detection, Catheter. Cardiovasc. Interv. 72 (2) (2008) 228–235.
[14] G.J. Ughi, T. Adriaenssens, K. Onsea, P. Kayaert, C. Dubois, P. Sinnaeve, et al., Automatic segmentation of in-vivo intra-coronary optical coherence tomography images to assess stent strut apposition and coverage, Int. J. Cardiovasc. Imaging 28 (2) (2011) 229–241.
[15] M.C. Moraes, D.A. Cardenas, S.S. Furuie, Automatic lumen segmentation in IVOCT images using binary morphological reconstruction, Biomed. Eng. Online 12 (2013) 78.
[16] S. Tsantis, G.C. Kagadis, K. Katsanos, D. Karnabatidis, G. Bourantas, G.C. Nikiforidis, Automatic vessel lumen segmentation and stent strut detection in intravascular optical coherence tomography, Med. Phys. 39 (1) (2012) 503–513.
[17] S. Gurmeric, G.G. Isguder, S. Carlier, G. Unal, A new 3-D automated computational method to evaluate in-stent neointimal hyperplasia in in-vivo intravascular optical coherence tomography pullbacks, Med. Image Comput. Comput. Assist. Interv. 12 (Pt 2) (2009) 776–785.
[18] R. Bourezak, G. Lamouche, F. Cheriet, Automatic Lumen Segmentation from Intravascular OCT Images. SPIE; http://dx.doi.org/10.1117/12.844316.
[19] L.S. Athanasiou, et al., Methodology for fully automated segmentation and plaque characterization in intracoronary optical coherence tomography images, J. Biomed. Opt. 19 (Feb (2)) (2014) 026009.
[20] S. Celi, S. Berti, In-vivo segmentation and quantification of coronary lesions by optical coherence tomography images for a lesion type definition and stenosis grading, Med. Image Anal. 18 (Oct (7)) (2014) 1157–1168.
[21] K. Sihan, et al., Fully automatic three-dimensional quantitative analysis of intracoronary optical coherence tomography: method and validation, Catheter. Cardiovasc. Interv. 74 (7) (2009) 1058–1065 Dec 1.
[22] Y.S. Chatzizisis, V. Koutkias, K. Toutouzas, A. Giannopoulos, I. Chouvarda, M. Riga, et al., Clinical validation of an algorithm for rapid and accurate automated segmentation of intracoronary optical coherence tomography images, Int. J. Cardiol. 172 (3) (2014) 568–580.
[23] M.S. Nixon, A.S. Aguado, Feature Extraction and Image Processing, second ed., Academic Press, 2008.
[24] M. Sezgin, B. Sankur, Survey over image thresholding techniques and quantitative performance evaluation, J. Electron. Imaging 13 (1) (2004) 146–165.
[25] W.S. Cleveland, Robust locally weighted regression and smoothing scatterplots, J. Am. Statist. Assoc. 74 (1) (1979) 829–836.
[26] M. Papadogiorgaki, V. Mezaris, Y.S. Chatzizisis, D.G. Giannoglou, I. Kompatsiaris, Image analysis techniques for automated IVUS contour detection, Ultrasound Med. Biol. 34 (9) (2008) 1482–1498.
[27] L.R. Dice, Measures of the amount of ecologic association between species, Ecology 26 (1945) 297–302.
[28] V. Chalana, Y. Kim, A methodology for evaluation of boundary detection algorithms on medical images, IEEE Trans. Med. Imaging 16 (5) (1997) 642–652.
[29] J.M. Bland, D.G. Altman, Statistical methods for assessing agreement between two methods of clinical measurement, The Lancet 327 (8476) (1986) 307–310.
[30] H.G. Bezerra, G.F. Attizzani, V. Sirbu, G. Musumeci, N. Lortkipanidze, Y. Fujino, et al., Optical coherence tomography versus intravascular ultrasound to evaluate coronary artery disease and percutaneous coronary intervention, JACC Cardiovasc. Interv. 6 (3) (2013) 228–236.
[31] C. Doulaverakis, I. Tsampoulatidis, A.P. Antoniadis, Y.S. Chatzizisis, A. Giannopoulos, I. Kompatsiaris, et al., IVUSAngio tool: a publicly available software for fast and accurate 3D reconstruction of coronary arteries, Comput. Biol. Med. 43 (11) (2013) 1793–1803.
[32] Y.S. Chatzizisis, A.U. Coskun, M. Jonas, E.R. Edelman, C.L. Feldman, P.H. Stone, Role of endothelial shear stress in the natural history of coronary atherosclerosis and vascular remodeling: molecular, cellular, and vascular behavior, J. Am. Coll. Cardiol. 49 (25) (2007) 2379–2393.